An E-J Collocated 3-D FDTD Model of Electromagnetic Wave Propagation in Magnetized Cold Plasma

Yaxin Yu, *Student Member, IEEE*, and Jamesina J. Simpson, *Member, IEEE*

Abstract—**A new three-dimensional finite-difference time-domain (FDTD) numerical model is proposed herein to simulate electromagnetic wave propagation in an anisotropic magnetized cold plasma medium. Plasma effects contributed by electrons, positive, and negative ions are considered in this model. The current density vectors are collocated at the positions of the electric field vectors, and the complete FDTD algorithm consists of three regular updating equations for the magnetic field intensity components, as well as 12 tightly coupled differential equations for updating the electric field components and current densities. This model has the capability to simulate wave behavior in magnetized cold plasma for an applied magnetic field with arbitrary direction and magnitude. We validate the FDTD algorithm by calculating Faraday rotation of a linearly polarized plane wave. Additional numerical examples of electromagnetic wave propagation in plasma are also provided, all of which demonstrate very good agreement with plasma theory.**

Index Terms—**Earth, electromagnetic wave propagation, finite-difference time-domain (FDTD) method, ionosphere, magnetized cold plasma.**

I. INTRODUCTION

OVER the past two decades, the finite-difference time-domain (FDTD) [1], [2] method has been extended to modeling electromagnetic (EM) wave propagation and interactions with cold plasmas. First, FDTD algorithms were developed for modeling nonmagnetized (therefore isotropic) cold plasma [3]–[9], or dispersive media FDTD algorithms were employed for isotropic plasma studies [10], [11]. A systematic analysis of these FDTD techniques has been published by S. A. Cummer [12].

An important aspect of plasma-related research is to study radio wave propagation through the ionosphere and to study lightning-related ionospheric phenomena. Many FDTD models have been developed to address these problems by treating the ionosphere as a simple nonmagnetized isotropic medium [13]–[15]. However, for accurate broadband investigations, effects introduced by the Earth's magnetic field on the ionospheric plasma cannot be ignored. Thus, a magnetized (anisotropic) cold plasma ionospheric medium must be employed in the FDTD simulations.

A few two-dimensional (2-D) and three-dimensional (3-D) FDTD models have been published that include the magnetic field effect on the ionospheric plasma. Cummer [16] proposed a 2-D cylindrical-coordinate FDTD model to study EM wave propagation in the Earth-ionosphere waveguide. Thèvenot *et al.* [17] reported another 2-D spherical-coordinate FDTD model to simulate VLF-LF propagation in the ionosphere. More recently, Hu and Cummer [18], [19] extended their full wave 2-D cylindrical coordinate FDTD model to explore lightning-generated EM wave behavior in the ionosphere and to test the sprite initiation theory. Unlike the H-J collocation method [20], the stability condition of Hu and Cummer's model involving the E-J collocation method is independent of medium properties and remains the same as for free space [12] (at the Courant stability limit [2]). This is a very important characteristic of their plasma algorithm. For some other FDTD plasma algorithms (see for example [21]–[23]), the time-stepping increment is linked to the plasma parameters, resulting in a strict time-step orders of magnitude smaller than that permitted by the Courant limit [2] when modeling the ionosphere [24], [25]. Further, some plasma algorithms, such as that of [21], produce nonphysically spurious electrostatic waves (of numerical origin) due to the spatially non-collocated status of electric fields and current densities [26] and thus exhibit seemingly incurable late-time instabilities when used to model ionospheric plasma, or they are only first-order accurate as for that proposed in [27], or their implementation requires a great amount of additional memory even for spatially unchanging plasma parameters as in [12], [28].

In this paper, we expand Hu and Cummer's 2-D E-J collocation FDTD model [18] to the fully 3-D case. As such, similar accuracy attained previously by Hu and Cummer for their 2-D model at both high altitudes and over long distances when compared to experiments and mode theory is expected here for the newly developed 3-D model. However, the 3-D model described in this paper provides additional capabilities, such as modeling of Faraday rotation and the inclusion of fully 3-D spatial variations in the magnetization and characteristics of the cold plasma. These capabilities are essential for future global 3-D studies of EM propagation and in many other research areas.

In Section II, the governing equations for the 3-D magnetized cold plasma are derived, as well as the resulting FDTD time-stepping algorithm. In Section III, the plasma FDTD model is validated, and Section IV illustrates some additional numerical examples of EM propagation in plasma. Finally, Section V concludes and describes ongoing work.

II. METHODOLOGY

A. Governing Equations

In the derivation of the 3-D FDTD magnetized cold plasma algorithm, wave propagation effects introduced by electrons, positive ions, and negative ions are included for generality. Here, we consider a cold plasma characterized by a free space permittivity ε_0 and a free space permeability μ_0 that is biased by an applied magnetic field $\mathbf{B}$. The magnetized cold plasma governing equations are cast in terms of Maxwell's equations coupled to current equations derived from the Lorentz equation of motion. The Lorentz current equations consist of three auxiliary partial differential equations that model the response of each charged particle species to the electric field $\mathbf{E}$ and the applied $\mathbf{B}$. The resulting whole governing equation set is given by

$$\nabla \times \mathbf{E} = -\mu_0 \frac{\partial \mathbf{H}}{\partial t} \tag{1}$$

$$\nabla \times \mathbf{H} = \varepsilon_0 \frac{\partial \mathbf{E}}{\partial t} + \mathbf{J}_I + \mathbf{J}_S \tag{2}$$

$$\frac{\partial \mathbf{J}_e}{\partial t} + v_e \mathbf{J}_e = \varepsilon_0 \omega_{Pe}^2 \mathbf{E} + \boldsymbol{\omega}_{Ce} \times \mathbf{J}_e \tag{3}$$

$$\frac{\partial \mathbf{J}_p}{\partial t} + v_p \mathbf{J}_p = \varepsilon_0 \omega_{Pp}^2 \mathbf{E} - \boldsymbol{\omega}_{Cp} \times \mathbf{J}_p \tag{4}$$

$$\frac{\partial \mathbf{J}_n}{\partial t} + v_n \mathbf{J}_n = \varepsilon_0 \omega_{Pn}^2 \mathbf{E} + \boldsymbol{\omega}_{Cn} \times \mathbf{J}_n \tag{5}$$

$$\mathbf{J}_I = \sum_l \mathbf{J}_l = \mathbf{J}_e + \mathbf{J}_p + \mathbf{J}_n. \tag{6}$$

Here the subscript l denotes the charged particle species in the plasma (e, p and n as electrons, positive ions, and negative ions, respectively). v_e, v_p and v_n are the collision frequencies of each species, and $\mathbf{J}_e$, $\mathbf{J}_p$ and $\mathbf{J}_n$ are the current densities of each species, respectively. $\mathbf{J}_S$ is the source current density. Cartesian coordinate expressions of these current densities are as below

$$\mathbf{J}_e = J_{ex}\hat{x} + J_{ey}\hat{y} + J_{ez}\hat{z} \tag{7}$$

$$\mathbf{J}_p = J_{px}\hat{x} + J_{py}\hat{y} + J_{pz}\hat{z} \tag{8}$$

$$\mathbf{J}_n = J_{nx}\hat{x} + J_{ny}\hat{y} + J_{nz}\hat{z} \tag{9}$$

$$\mathbf{J}_S = J_{Sx}\hat{x} + J_{Sy}\hat{y} + J_{Sz}\hat{z}. \tag{10}$$

The total induced charged-particle current density $\mathbf{J}_I$ is then the combination of all three of the individual current densities as shown in (6) and the sum of $\mathbf{J}_I$ and $\mathbf{J}_S$ forms the total current density as in (2). Further, ω_{Pe}, ω_{Pp} and ω_{Pn} are the plasma frequencies of each species, respectively. By construction

$$\omega_{pl} = \sqrt{\frac{q_l^2 n_l}{\varepsilon_0 m_l}} \tag{11}$$

with q_l, n_l and m_l as the charge, number density, and mass of each particle species. In addition $\boldsymbol{\omega}_{Ce}$, $\boldsymbol{\omega}_{Cp}$ and $\boldsymbol{\omega}_{Cn}$ are the cyclotron frequencies of each species given by $\boldsymbol{\omega}_{Cl} = q_l \mathbf{B}/m_l$ with Cartesian coordinate expressions

$$\boldsymbol{\omega}_{Ce} = \omega_{Cex}\hat{x} + \omega_{Cey}\hat{y} + \omega_{Cez}\hat{z} \tag{12}$$

$$\boldsymbol{\omega}_{Cp} = \omega_{Cpx}\hat{x} + \omega_{Cpy}\hat{y} + \omega_{Cpz}\hat{z} \tag{13}$$

$$\boldsymbol{\omega}_{Cn} = \omega_{Cnx}\hat{x} + \omega_{Cny}\hat{y} + \omega_{Cnz}\hat{z} \tag{14}$$

Notice that the cyclotron frequency is a function of the applied magnetic field. Thus, the cross-product terms in (3)–(5) make the plasma anisotropic so that the wave behavior depends on its propagation direction relative to the direction of the magnetic field. Without these cross product terms, the whole system of (1)–(6) simply becomes the governing equation set of a nonmagnetized (isotropic) cold plasma.

By substituting (7)–(14) into (1)–(6) and separating out each Cartesian expression, the whole governing differential equation set is expanded into 15 scalar equations

$$\frac{\partial Hx}{\partial t} = \frac{1}{\mu_0}\left[\frac{\partial Ey}{\partial z} - \frac{\partial Ez}{\partial y}\right] \tag{15}$$

$$\frac{\partial Hy}{\partial t} = \frac{1}{\mu_0}\left[\frac{\partial Ez}{\partial x} - \frac{\partial Ex}{\partial z}\right] \tag{16}$$

$$\frac{\partial Hz}{\partial t} = \frac{1}{\mu_0}\left[\frac{\partial Ex}{\partial y} - \frac{\partial Ey}{\partial x}\right] \tag{17}$$

$$\frac{\partial Ex}{\partial t} = \frac{1}{\varepsilon_0}\left[\frac{\partial Hz}{\partial y} - \frac{\partial Hy}{\partial z} - J_{ex} - J_{px} - J_{nx} - J_{Sx}\right] \tag{18}$$

$$\frac{\partial Ey}{\partial t} = \frac{1}{\varepsilon_0}\left[\frac{\partial Hx}{\partial z} - \frac{\partial Hz}{\partial x} - J_{ey} - J_{py} - J_{ny} - J_{Sy}\right] \tag{19}$$

$$\frac{\partial Ez}{\partial t} = \frac{1}{\varepsilon_0}\left[\frac{\partial Hy}{\partial x} - \frac{\partial Hx}{\partial y} - J_{ez} - J_{pz} - J_{nz} - J_{Sz}\right] \tag{20}$$

$$\frac{dJ_{ex}}{dt} + v_e J_{ex} = \varepsilon_0 \omega_{Pe}^2 E_x + \omega_{Cey} J_{ez} - \omega_{Cez} J_{ey} \tag{21}$$

$$\frac{dJ_{ey}}{dt} + v_e J_{ey} = \varepsilon_0 \omega_{Pe}^2 E_y + \omega_{Cez} J_{ex} - \omega_{Cex} J_{ez} \tag{22}$$

$$\frac{dJ_{ez}}{dt} + v_e J_{ez} = \varepsilon_0 \omega_{Pe}^2 E_z + \omega_{Cex} J_{ey} - \omega_{Cey} J_{ex} \tag{23}$$

$$\frac{dJ_{px}}{dt} + v_p J_{px} = \varepsilon_0 \omega_{Pp}^2 E_x + \omega_{Cpz} J_{py} - \omega_{Cpy} J_{pz} \tag{24}$$

$$\frac{dJ_{py}}{dt} + v_p J_{py} = \varepsilon_0 \omega_{Pp}^2 E_y + \omega_{Cpx} J_{pz} - \omega_{Cpz} J_{px} \tag{25}$$

$$\frac{dJ_{pz}}{dt} + v_p J_{pz} = \varepsilon_0 \omega_{Pp}^2 E_z + \omega_{Cpy} J_{px} - \omega_{Cpx} J_{py} \tag{26}$$

$$\frac{dJ_{nx}}{dt} + v_n J_{nx} = \varepsilon_0 \omega_{Pn}^2 E_x + \omega_{Cny} J_{nz} - \omega_{Cnz} J_{ny} \tag{27}$$

$$\frac{dJ_{ny}}{dt} + v_n J_{ny} = \varepsilon_0 \omega_{Pn}^2 E_y + \omega_{Cnz} J_{nx} - \omega_{Cnx} J_{nz} \tag{28}$$

$$\frac{dJ_{nz}}{dt} + v_n J_{nz} = \varepsilon_0 \omega_{Pn}^2 E_z + \omega_{Cnx} J_{ny} - \omega_{Cny} J_{nx}. \tag{29}$$

B. FDTD Discretization Scheme

In this Section, the 15 scalar equations of (15)–(29) are applied to the FDTD mesh. Here, we adopt the E-J collocation method as described in [12]. This locates the J_x, J_y, and J_z components at the same positions of E_x, E_y, and E_z, respectively. The Yee cell describing the spatial positioning of the electric, magnetic, and current density field vector components is shown in Fig. 1. For central differencing of the space derivatives in (15)–(29), we define a sample E_x and J_x at $(i + 1/2, j, k)$, E_y and J_y at $(i, j + 1/2, k)$, E_z and J_z at $(i, j, k + 1/2)$, H_x at $(i, j + 1/2, k + 1/2)$, H_y at $(i + 1/2, j, k + 1/2)$ and H_z at $(i + 1/2, j + 1/2, k)$.

The 3-D magnetized plasma FDTD updating equations of the $\mathbf{H}$-fields derived from (15)–(17) are identical to those of the standard Yee algorithm [2]. Equation (30) provides a sample
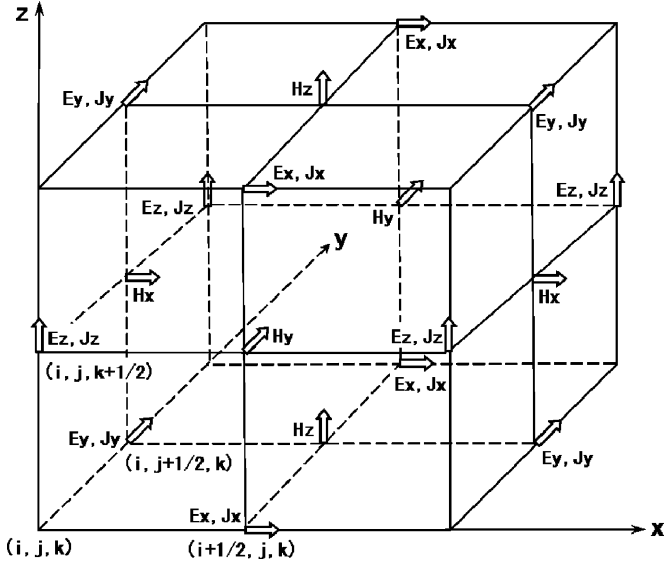
Fig. 1. Yee cell for spatial positioning of the field components.

updating algorithm of the H_x component as derived from (15) and the spatial scheme of Fig. 1.

Then, referring to Fig. 1 and using the so-called semi-implicit approximation [2], the 12 E- and J-related equations of (18)–(29) can be discretized first at the x-component position $(i + 1/2, j, k)$. The 12 resulting tightly-coupled discretization equations can then be written in matrix form as expressed in

(31), shown at the bottom of the page. The corresponding coefficient of each field component is then grouped into the three coefficient matrixes $A[12 \times 12]$, $B[12 \times 12]$ and $C[12 \times 9]$, which are detailed in Appendix for reference. Where $\hat{H}_u = (\mu_0 \Delta u / \Delta t) H_u$ $[u = x, y, z]$ and $\hat{J} = (\Delta t / \varepsilon_0) J$ are scaled values of the original magnetic field intensity H and current density J. These scaled field values are actual quantities used for updating $\mathbf{E}$ and $\mathbf{J}$ during the iteration. This scaling is required to avoid instability and inaccuracies that would result from the large iteration coefficients [18]. $\mathbf{E}$ is not scaled.

Working towards an explicit expression, both sides of (31) are multiplied by the inverse matrix A^{-1} to be transformed into (32), shown at the bottom of the following page, which yields all of the field components at time-step $(n + 1)$ on the left-hand side of (32) and all of the field values calculated at previous time steps on the right-hand side of (32). This results in (32) to be an explicit system suitable for FDTD implementation. In space domain, all of these field quantities are now assumed to be located at x-component position $(i + 1/2, j, k)$, we therefore name (32) as the X-equation. The same process can then be repeated at the y-component position $(i, j + 1/2, k)$ and z-component position $(i, j, k + 1/2)$ to obtain the Y-equation and Z-equation, respectively. These three explicit matrix equations are very similar except different spatial positions of the field quantities and derivatives.

We next notice that all of the non-x field-components in the X-equation (32) have no field values defined at x-component location $(i + 1/2, j, k)$ according to our leapfrog scheme in Fig. 1,

$$H_x\big|_{i,\,j+1/2,\,k+1/2}^{n+1/2} = H_x\big|_{i,\,j+1/2,\,k+1/2}^{n-1/2} + \frac{\Delta t}{\mu_0}\left[\frac{E_y\big|_{i,\,j+1/2,\,k+1}^{n} - E_y\big|_{i,\,j+1/2,\,k}^{n}}{\Delta z} - \frac{E_z\big|_{i,\,j+1,\,k+1/2}^{n} - E_z\big|_{i,\,j,\,k+1/2}^{n}}{\Delta y}\right]. \quad (30)$$

$$[A] \cdot \begin{bmatrix} E_x\big|_{i+1/2,j,k}^{n+1} \\ E_y\big|_{i+1/2,j,k}^{n+1} \\ E_z\big|_{i+1/2,j,k}^{n+1} \\ \hat{J}_{ex}\big|_{i+1/2,j,k}^{n+1} \\ \hat{J}_{px}\big|_{i+1/2,j,k}^{n+1} \\ \hat{J}_{nx}\big|_{i+1/2,j,k}^{n+1} \\ \hat{J}_{ey}\big|_{i+1/2,j,k}^{n+1} \\ \hat{J}_{py}\big|_{i+1/2,j,k}^{n+1} \\ \hat{J}_{ny}\big|_{i+1/2,j,k}^{n+1} \\ \hat{J}_{ez}\big|_{i+1/2,j,k}^{n+1} \\ \hat{J}_{pz}\big|_{i+1/2,j,k}^{n+1} \\ \hat{J}_{nz}\big|_{i+1/2,j,k}^{n+1} \end{bmatrix} = [B] \cdot \begin{bmatrix} E_x\big|_{i+1/2,j,k}^{n} \\ E_y\big|_{i+1/2,j,k}^{n} \\ E_z\big|_{i+1/2,j,k}^{n} \\ \hat{J}_{ex}\big|_{i+1/2,j,k}^{n} \\ \hat{J}_{px}\big|_{i+1/2,j,k}^{n} \\ \hat{J}_{nx}\big|_{i+1/2,j,k}^{n} \\ \hat{J}_{ey}\big|_{i+1/2,j,k}^{n} \\ \hat{J}_{py}\big|_{i+1/2,j,k}^{n} \\ \hat{J}_{ny}\big|_{i+1/2,j,k}^{n} \\ \hat{J}_{ez}\big|_{i+1/2,j,k}^{n} \\ \hat{J}_{pz}\big|_{i+1/2,j,k}^{n} \\ \hat{J}_{nz}\big|_{i+1/2,j,k}^{n} \end{bmatrix} + [C] \cdot \begin{bmatrix} \left(\frac{\Delta \hat{H}_z}{\Delta y}\right)_{i+1/2,j,k}^{n+1/2} \\ \left(\frac{\Delta \hat{H}_y}{\Delta z}\right)_{i+1/2,j,k}^{n+1/2} \\ \left(\frac{\Delta \hat{H}_x}{\Delta z}\right)_{i+1/2,j,k}^{n+1/2} \\ \left(\frac{\Delta \hat{H}_z}{\Delta x}\right)_{i+1/2,j,k}^{n+1/2} \\ \left(\frac{\Delta \hat{H}_y}{\Delta x}\right)_{i+1/2,j,k}^{n+1/2} \\ \left(\frac{\Delta \hat{H}_x}{\Delta y}\right)_{i+1/2,j,k}^{n+1/2} \\ \hat{J}_{Sx}\big|_{i+1/2,j,k}^{n+1/2} \\ \hat{J}_{Sy}\big|_{i+1/2,j,k}^{n+1/2} \\ \hat{J}_{Sz}\big|_{i+1/2,j,k}^{n+1/2} \end{bmatrix}. \quad (31)$$

which makes the direct implementing of the non-x field-quantities in first column of the X-equation (32) at their pre-defined Yee-locations impossible. The same situation happens to the non-y field-quantities of the Y-equation and the non-z field-quantities of the Z-equation, similarly.

Notice that the coefficient matrix $A^{-1}B$ and $A^{-1}C$ are analogous for the X-, Y- and Z-equations, we then pick up the 4 linear x-component updating equations from the X-equation ($E_x|_{i+1/2,j,k}^{n+1}, \widehat{J}_{ex}|_{i+1/2,j,k}^{n+1}, \widehat{J}_{px}|_{i+1/2,j,k}^{n+1}, \widehat{J}_{nx}|_{i+1/2,j,k}^{n+1},$) the 4 linear y-component updating equations from the Y-equation ($E_y|_{i,j+1/2,k}^{n+1}, \widehat{J}_{ey}|_{i,j+1/2,k}^{n+1}, \widehat{J}_{py}|_{i,j+1/2,k}^{n+1}, \widehat{J}_{ny}|_{i,j+1/2,k}^{n+1}$) and the 4 z-component updating equations from the Z-equation ($E_z|_{i,j,k+1/2}^{n+1}, \widehat{J}_{ez}|_{i,j,k+1/2}^{n+1}, \widehat{J}_{pz}|_{i,j,k+1/2}^{n+1}, \widehat{J}_{nz}|_{i,j,k+1/2}^{n+1},$) to be recombined to obtain a new explicit equation (33), which is the eventual iteration set used to implement the whole system. The field quantities in the first column of (33) are now all positioned at their pre-defined spatial locations, which allow them to be linearly direct-implemented. To update the

x-components, all of the field quantities and derivatives at the right-hand side of (33) need to be evaluated at $(i+1/2,j,k)$ just as shown in (32). Similarly, for updating the y-components and z-components in the first column of (33), these quantities then need to be calculated at $(i,j+1/2,k)$ and $(i,j,k+1/2)$, respectively. This makes the spatial indices impossible to be explicitly expressed for the field quantities and derivatives on the right-hand side of (33) and they are therefore only denoted in time domain.

The iteration coefficients needed for implementation are then the matrix elements in $A^{-1}B$ and $A^{-1}C$, which only depend on the plasma properties and the modeling parameters. For time-invariant homogeneous plasma, these coefficients are only needed to be calculated once. For inhomogeneous medium such as ionospheric plasma, these coefficients vary with height and position around the Earth, and additional calculations and storage are therefore required to account for the location-dependence of the parameters. However, these additional coefficients may

$$
\begin{bmatrix}
E_x|_{i+1/2,j,k}^{n+1} \\
E_y|_{i+1/2,j,k}^{n+1} \\
E_z|_{i+1/2,j,k}^{n+1} \\
\widehat{J}_{ex}|_{i+1/2,j,k}^{n+1} \\
\widehat{J}_{px}|_{i+1/2,j,k}^{n+1} \\
\widehat{J}_{nx}|_{i+1/2,j,k}^{n+1} \\
\widehat{J}_{ey}|_{i+1/2,j,k}^{n+1} \\
\widehat{J}_{py}|_{i+1/2,j,k}^{n+1} \\
\widehat{J}_{ny}|_{i+1/2,j,k}^{n+1} \\
\widehat{J}_{ez}|_{i+1/2,j,k}^{n+1} \\
\widehat{J}_{pz}|_{i+1/2,j,k}^{n+1} \\
\widehat{J}_{nz}|_{i+1/2,j,k}^{n+1}
\end{bmatrix}
= \left[A^{-1}B\right] \cdot
\begin{bmatrix}
E_x|_{i+1/2,j,k}^{n} \\
E_y|_{i+1/2,j,k}^{n} \\
E_z|_{i+1/2,j,k}^{n} \\
\widehat{J}_{ex}|_{i+1/2,j,k}^{n} \\
\widehat{J}_{px}|_{i+1/2,j,k}^{n} \\
\widehat{J}_{nx}|_{i+1/2,j,k}^{n} \\
\widehat{J}_{ey}|_{i+1/2,j,k}^{n} \\
\widehat{J}_{py}|_{i+1/2,j,k}^{n} \\
\widehat{J}_{ny}|_{i+1/2,j,k}^{n} \\
\widehat{J}_{ez}|_{i+1/2,j,k}^{n} \\
\widehat{J}_{pz}|_{i+1/2,j,k}^{n} \\
\widehat{J}_{nz}|_{i+1/2,j,k}^{n}
\end{bmatrix}
+ \left[A^{-1}C\right] \cdot
\begin{bmatrix}
\left(\frac{\Delta \widehat{H}_z}{\Delta y}\right)_{i+1/2,j,k}^{n+1/2} \\
\left(\frac{\Delta \widehat{H}_y}{\Delta z}\right)_{i+1/2,j,k}^{n+1/2} \\
\left(\frac{\Delta \widehat{H}_x}{\Delta z}\right)_{i+1/2,j,k}^{n+1/2} \\
\left(\frac{\Delta \widehat{H}_z}{\Delta x}\right)_{i+1/2,j,k}^{n+1/2} \\
\left(\frac{\Delta \widehat{H}_y}{\Delta x}\right)_{i+1/2,j,k}^{n+1/2} \\
\left(\frac{\Delta \widehat{H}_x}{\Delta y}\right)_{i+1/2,j,k}^{n+1/2} \\
\widehat{J}_{Sx}|_{i+1/2,j,k}^{n+1/2} \\
\widehat{J}_{Sy}|_{i+1/2,j,k}^{n+1/2} \\
\widehat{J}_{Sz}|_{i+1/2,j,k}^{n+1/2}
\end{bmatrix}
\tag{32}
$$

$$
\begin{bmatrix}
E_x|_{i+1/2,j,k}^{n+1} \\
E_y|_{i,j+1/2,k}^{n+1} \\
E_z|_{i,j,k+1/2}^{n+1} \\
\widehat{J}_{ex}|_{i+1/2,j,k}^{n+1} \\
\widehat{J}_{px}|_{i+1/2,j,k}^{n+1} \\
\widehat{J}_{nx}|_{i+1/2,j,k}^{n+1} \\
\widehat{J}_{ey}|_{i,j+1/2,k}^{n+1} \\
\widehat{J}_{py}|_{i,j+1/2,k}^{n+1} \\
\widehat{J}_{ny}|_{i,j+1/2,k}^{n+1} \\
\widehat{J}_{ez}|_{i,j,k+1/2}^{n+1} \\
\widehat{J}_{pz}|_{i,j,k+1/2}^{n+1} \\
\widehat{J}_{nz}|_{i,j,k+1/2}^{n+1}
\end{bmatrix}
= \left[A^{-1}B\right] \cdot
\begin{bmatrix}
E_x^n \\
E_y^n \\
E_z^n \\
\widehat{J}_{ex}^n \\
\widehat{J}_{px}^n \\
\widehat{J}_{nx}^n \\
\widehat{J}_{ey}^n \\
\widehat{J}_{py}^n \\
\widehat{J}_{ny}^n \\
\widehat{J}_{ez}^n \\
\widehat{J}_{pz}^n \\
\widehat{J}_{nz}^n
\end{bmatrix}
+ \left[A^{-1}C\right] \cdot
\begin{bmatrix}
\left(\frac{\Delta \widehat{H}_z}{\Delta y}\right)^{n+1/2} \\
\left(\frac{\Delta \widehat{H}_y}{\Delta z}\right)^{n+1/2} \\
\left(\frac{\Delta \widehat{H}_x}{\Delta z}\right)^{n+1/2} \\
\left(\frac{\Delta \widehat{H}_z}{\Delta x}\right)^{n+1/2} \\
\left(\frac{\Delta \widehat{H}_y}{\Delta x}\right)^{n+1/2} \\
\left(\frac{\Delta \widehat{H}_x}{\Delta y}\right)^{n+1/2} \\
\widehat{J}_{Sx}^{n+1/2} \\
\widehat{J}_{Sy}^{n+1/2} \\
\widehat{J}_{Sz}^{n+1/2}
\end{bmatrix}
\tag{33}
$$

be efficiently pre-calculated and stored before time-stepping to be used during the iteration.

It is important to note that for this method, spatial-averaging is required for all of the spatially non-collocated state variables and derivatives to maintain the algorithm second-order accuracy. For example, to update $E_x|_{i+1/2, j, k}^{n+1}$ through (33), all of the field quantities and derivatives at the right-hand side of (33) need to be evaluated at $(i + 1/2, j, k)$ as mentioned above. However, according to our leapfrog scheme in Fig. 1, there are no pre-defined field values at this precise location for E_y^n, E_z^n, $\hat{J}_{ey}^n$, $\hat{J}_{py}^n$, $\hat{J}_{ny}^n$, $\hat{J}_{ez}^n$, $\hat{J}_{pz}^n$, $\hat{J}_{nz}^n$, $\hat{J}_{Sy}^{n+1/2}$, $\hat{J}_{Sz}^{n+1/2}$, $(\Delta \hat{H}_x / \Delta z)^{n+1/2}$, $(\Delta \hat{H}_z / \Delta x)^{n+1/2}$, $(\Delta \hat{H}_y / \Delta x)^{n+1/2}$ and $(\Delta \hat{H}_x / \Delta y)^{n+1/2}$. For the spatially non-collocated E and $\hat{J}$ components above, four neighboring diagonal field values are thus averaged about $(i + 1/2, j, k)$ in order to find the field value at that position. As an example, the spatial averaging of $\hat{J}_{ey}$ is illustrated in Fig. 2 and expressed as (34). For the spatially non-collocated derivatives listed above, eight cubic diagonal field values surrounding $(i + 1/2, j, k)$ are then utilized to evaluate the corresponding derivative at that point. As an example, the spatial averaging of derivative $(\Delta \hat{H}_x / \Delta z)^{n+1/2}$ is illustrated in Fig. 3 and expressed as (35). All of the other spatially non-collocated field quantities are treated in a similar manner where spatial-averaging is needed.

The iteration process of the whole system is realized by first updating the **H**-field components through the three regular discretized FDTD equations from (15)–(17), scaling the **H**-fields, then updating the **E**- and **J**-field components through (33), de-scaling the **H**-fields, and finally repeating this process in the next iteration loop.

C. Stability and Accuracy Analysis of the Scheme

Unlike the H-J collocation method [20] and the algorithm in [21], the most appreciable advantage of this E-J collocation method is that the stability condition is independent of plasma properties, which is a crucial characteristic when modeling the ionosphere. The maximum stable Courant number in unmagnetized cold plasma for the E-J collocation method is unity just as
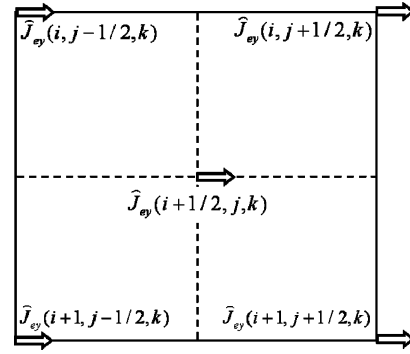

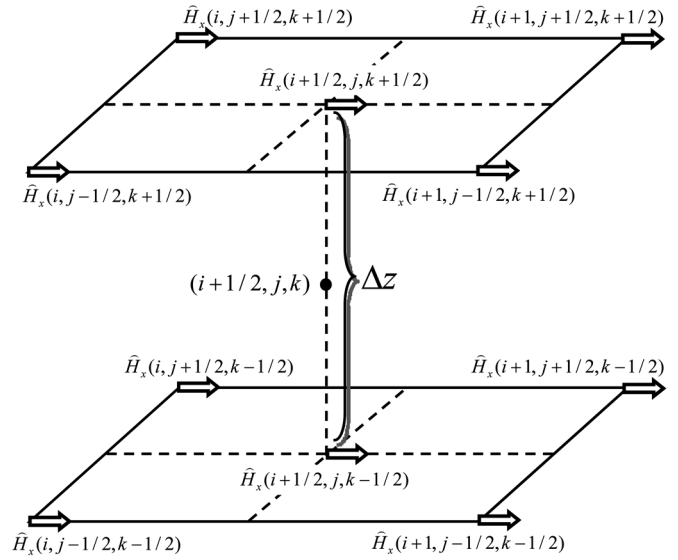Fig. 2. The illustration of the spatial averaging of $\bar{J}_{ey}$.

Fig. 3. The illustration of the spatial averaging of $(\Delta \bar{H}_x / \Delta z)^{n+1/2}$.

for free space [12]. For magnetized plasma medium, the effect of the anisotropy on the stability of the FDTD scheme is less predictable due to the complexity of the algorithm. It has been

$$\hat{J}_{ey}|_{i+1/2, j, k}^{n} = \frac{\hat{J}_{ey}|_{i, j-1/2, k}^{n} + \hat{J}_{ey}|_{i, j+1/2, k}^{n} + \hat{J}_{ey}|_{i+1, j+1/2, k}^{n} + \hat{J}_{ey}|_{i+1, j-1/2, k}^{n}}{4} \tag{34}$$

$$\left.\frac{\Delta \hat{H}_x}{\Delta z}\right|_{i+1/2, j, k}^{n+1/2} = \frac{\hat{H}_x|_{i+1/2, j, k+1/2}^{n+1/2} - \hat{H}_x|_{i+1/2, j, k-1/2}^{n+1/2}}{\Delta z}$$

$$= \frac{\left[\frac{\left(\hat{H}_x|_{i, j+1/2, k+1/2}^{n+1/2} + \hat{H}_x|_{i+1, j+1/2, k+1/2}^{n+1/2} + \hat{H}_x|_{i+1, j-1/2, k+1/2}^{n+1/2} + \hat{H}_x|_{i, j-1/2, k+1/2}^{n+1/2}\right)}{4} - \frac{\left(\hat{H}_x|_{i, j+1/2, k-1/2}^{n+1/2} + \hat{H}_x|_{i+1, j+1/2, k-1/2}^{n+1/2} + \hat{H}_x|_{i+1, j-1/2, k-1/2}^{n+1/2} + \hat{H}_x|_{i, j-1/2, k-1/2}^{n+1/2}\right)}{4}\right]}{\Delta z} \tag{35}$$

found empirically that the stability condition in the unmagnetized case is still valid for the magnetized case [18], which has been verified by our numerical results as well as the numerical experiments presented in [17].

Due to the semi-implicit differencing of the current density terms in (21)–(29), $\nu\Delta t \ll 1$ and $\omega_c\Delta t \ll 1$ must hold theoretically to maintain accuracy. However, as shown in the dispersion analysis of [12], the accuracy of this E-J collocation method is comparable to other differencing methods even for $\nu\Delta t \sim 1$ in unmagnetized cold plasma. Additionally, for both the unmagnetized and magnetized cases, $\nu\Delta t < 2$ must hold to approximate the analytical solutions of the original differential equations (21)–(29) since the homogeneous solutions of the semi-implicit differencing equations of (21)-(29) have a growth per time-step factor of $(1 - \nu\Delta t/2)/(1 + \nu\Delta t/2)$. Therefore, for the magnetized case, a suitable spatial grid-cell size must be carefully chosen to satisfy both the stability condition and accuracy requirements. Criteria for choosing this grid-cell size may be obtained through dispersion analysis, however it is very complex due to the anisotropy and will not be shown here. In general, we see the E-J collocation method as having a major advantage over other algorithms, because the grid parameters may be chosen based on the Courant stability limit, and only further reduced to the level that provides an acceptable level of accuracy, as done in [18] for wave propagation in the ionosphere (as opposed to being forced to use a time step dependent on the plasma's parameters [24] when implementing the method of [21], which results in a time step three orders of magnitude smaller than that imposed by the Courant limit [25]).

III. VALIDATION OF THE ALGORITHM

Having a fully 3-D cold plasma model, we choose to validate our FDTD algorithm by testing the Faraday rotation effect in a lossless electron plasma without ions. According to plasma theory [29], a linearly polarized plane wave propagating in a direction parallel to the direction of the applied magnetic field will be decomposed to a right-hand (RH) and a left-hand (LH) circularly polarized wave with different phase velocities. This causes the plane of polarization of the linearly polarized wave to rotate as the wave propagates through the plasma. The rotation angle per unit distance θ_F can be written as

$$\theta_F = \frac{\theta_t}{d} = \frac{\beta_{LH} - \beta_{RH}}{2} \qquad (36)$$

where θ_t is the total rotation angle over a distance d. β_{LH} and β_{RH} are the propagation constants for the LH- and RH- polarized wave, respectively. By construction

$$\beta_{LH} = \omega(\mu_0\varepsilon_0)^{1/2}\sqrt{1 - \frac{\frac{\omega_{pe}^2}{\omega}}{\omega_{ce} + \omega}} \qquad (37)$$

$$\beta_{RH} = \omega(\mu_0\varepsilon_0)^{1/2}\sqrt{1 + \frac{\frac{\omega_{pe}^2}{\omega}}{\omega_{ce} - \omega}}. \qquad (38)$$

Here, ω_{pe} and ω_{ce} are the plasma frequency and cyclotron frequency of the electrons, respectively. ω is the frequency of the linearly polarized plane wave.

We test the Faraday rotation effect by sending an initially x-polarized unit sinusoidal plane wave into the plasma. The
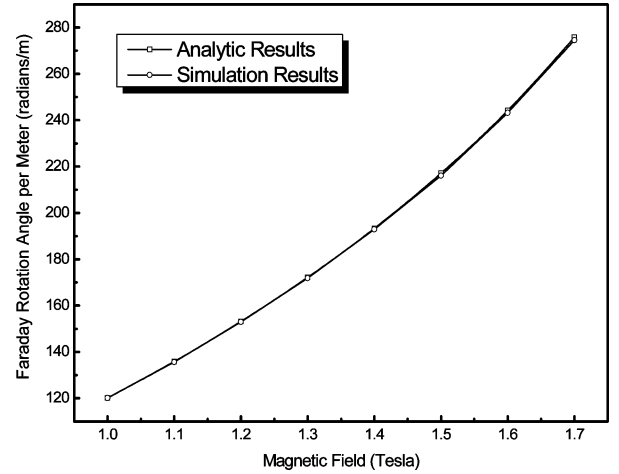

Fig. 4.   The comparison of the simulated and analytical results of the Faraday rotation angle per meter.

wave propagation and the applied magnetic field are both along z-coordinate. The simulation parameters are

$$\Delta x = \Delta y = \Delta z = 75\ \mu m \qquad (39)$$

$$\Delta t = 0.125\ \text{ps} \qquad (40)$$

$$\omega_{pe} = 3.14 \times 10^{11}\ \frac{\text{rad}}{\text{s}} \qquad (41)$$

$$\omega = 5.718 \times 10^{11}\ \frac{\text{rad}}{\text{s}}. \qquad (42)$$

Each simulation is run for 1750 time steps and repeated for magnetic field values ranging from 1.0 to 1.7 Tesla. The electric field components E_x and E_y are recorded at several distances away from the source plane wave. The FDTD-calculated Faraday rotation angle per unit distance θ_F for each magnetic field value is then given by

$$\theta_F = \frac{\theta_t}{d} = \frac{\tan^{-1}\left(\frac{E_y}{E_x}\right)}{d}. \qquad (43)$$

In Fig. 4, the simulation results of (43) are compared with the analytical results of (36). The FDTD simulation results are seen to be in very good agreement with the analytical results with an average error of 0.0031%. The average error is defined as

$$\text{error} = \frac{\sum\limits_n |\theta_{FS} - \theta_{FA}|}{\sum\limits_n |\theta_{FA}|} \qquad (44)$$

where θ_{FS} and θ_{FA} are the simulated and analytical Faraday rotation angles per unit distance, respectively, and, n is the sampling numbers. In our case $n = 8$.

To demonstrate the Faraday rotation effect, tracings of the total electric field vectors at different recording points along the direction of propagation for the $B = 1.7T$ case are illustrated in Fig. 5. These tracings show the rotation of the linearly polarized wave, and they are obtained by plotting the recorded E_x and E_y values over one cycle using the electric field magnitudes as the x-y coordinates. The initial plane of polarization of the linearly polarized wave is along x-coordinate. As the wave propagates through the plasma, it starts rotating as shown in Fig. 5 with a constant rotation angle per unit distance stated in (36). Due to
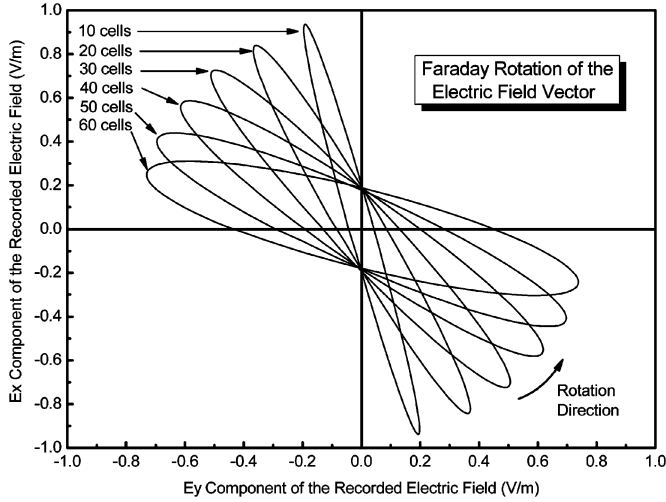
Fig. 5. Demonstration of the Faraday rotation effect.

IV. NUMERICAL DEMONSTRATIONS OF ELECTROMAGNETIC WAVE PROPAGATION IN THE PLASMA

In this Section, the 3-D FDTD cold plasma model is used to further demonstrate EM propagation characteristics in a lossless plasma medium. We again generate an x-polarized Gaussian-pulsed plane wave propagating along the externally applied magnetic field. The Gaussian pulse is described by

$$E_x = \exp\left[\frac{-(t - 50\Delta t)^2}{2(7\Delta t)^2}\right]. \tag{45}$$

We first model the plasma as having an electron density of 1.0×10^{18} m^{-3} without ions under an applied 0.06T magnetic field. Thus the simulation is characterized by

$$\text{electron plasma frequency}: \omega_{pe} = 5.64 \times 10^{10} \frac{\text{rad}}{\text{s}} \tag{46}$$

$$\text{electron cyclotron frequency}: \omega_{ce} = 1.06 \times 10^{10} \frac{\text{rad}}{\text{s}} \tag{47}$$

$$\text{LHC cutoff frequency}: \omega_L = 5.14 \times 10^{10} \frac{\text{rad}}{\text{s}} \tag{48}$$

$$\text{RHC cutoff frequency}: \omega_R = 6.19 \times 10^{10} \frac{\text{rad}}{\text{s}} \tag{49}$$

$$\Delta x = \Delta y = \Delta z = 1 \text{ mm} \tag{50}$$

$$\Delta t = 1.8346 \text{ ps}. \tag{51}$$

Fig. 6 illustrates the time and frequency domain waveforms of E_x at the recording point located 40 cells away from the sourced plane wave. Clearly shown in the frequency domain waveform as in Fig. 6(b) is the slow whistler mode below the electron cyclotron frequency, and a resonance at the cyclotron frequency. The slow whistler mode is observed in the time-domain results in Fig. 6(a) as a low frequency oscillation arriving at about 600 time-steps. Above the stop band extending between the electron cyclotron frequency and the LHC cutoff frequency (for our case
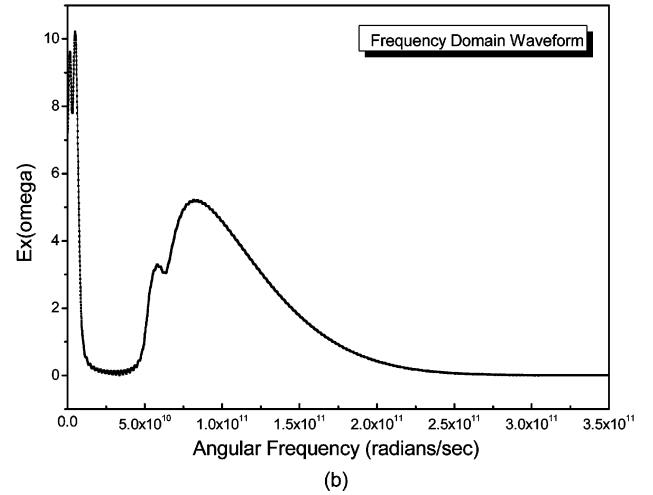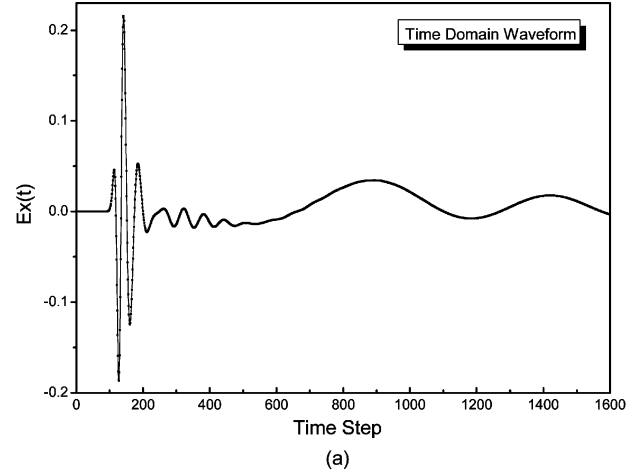

Fig. 6. Waveforms for a Gaussian-pulsed plane wave propagating in the plasma with an applied magnetic field (a) Time Domain and (b) Frequency Domain.

of $\omega_L < \omega_P$), the LH- and RH-circularly polarized modes are observed with distinct cutoffs at ω_L and ω_R, respectively. These numerical results of our 3-D FDTD model agree very well with plasma theory.

We next repeat the above experiment, but without the applied magnetic field. The solid lines in Fig. 7 illustrate the results of this second case having only electrons. The cutoff at the electron plasma frequency is clearly shown in the frequency domain waveform of Fig. 7(b). Further a long tail oscillating at the electron plasma frequency is observed in the time domain waveform of Fig. 7(a). This results from the very slow group velocities near the cutoff frequency.

As a final test, we introduce a positive ion species of O$_2^+$ with atomic mass 32 into our model to study the impact of having a plasma comprised of both ions and electrons. The ion density is 1.0×10^{22} m^{-3} and all other parameters are kept the same as in the electron-only case above. The ion plasma frequency ω_{pi} and the total plasma frequency ω_p are then given by

$$\omega_{pi} = 2.34 \times 10^{10} \frac{\text{rad}}{\text{s}} \tag{52}$$

$$\omega_p = \sqrt{\omega_{pe}^2 + \omega_{pi}^2} = 6.11 \times 10^{10} \frac{\text{rad}}{\text{s}}. \tag{53}$$
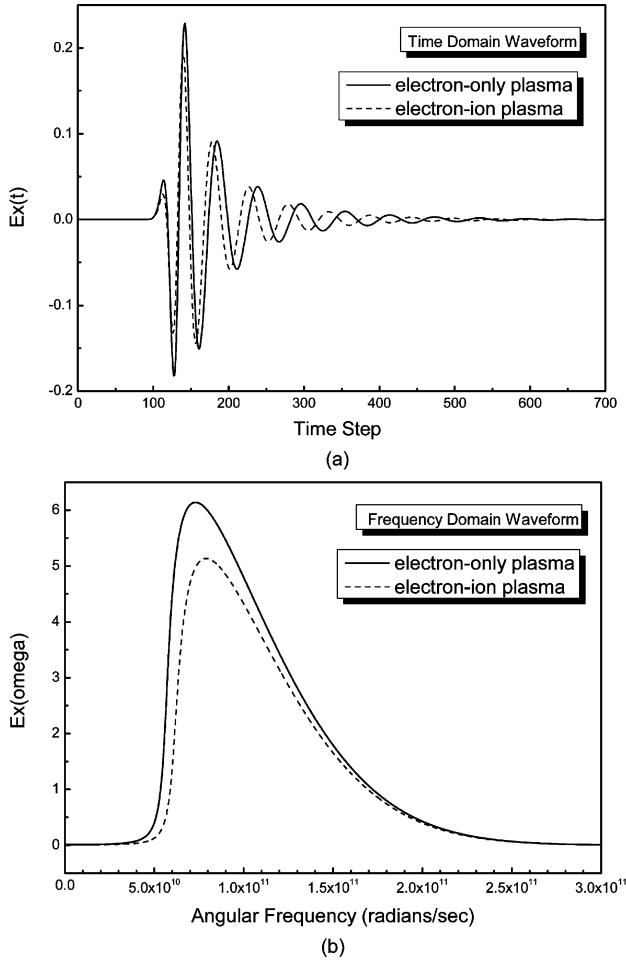
Fig. 7. Waveforms for a Gaussian-pulsed plane wave propagating in the plasma without external magnetic field (a) Time Domain (b) Frequency Domain.

The dashed lines of Fig. 7 illustrate the results of this third test plasma case including both ions and electrons. The oscillating frequency of the time-domain tail has clearly increased from ω_{pe} of the electron-only plasma case to ω_p as shown in Fig. 7(a) and the frequency-domain cutoff has also shifted from ω_{pe} to ω_p as

observed in Fig. 7(b). Again, these numerical results agree with plasma theory very well.

V. CONCLUSION AND ONGOING WORK

We report a 3-D FDTD model of EM wave propagation in anisotropic magnetized cold plasma. This model is based upon the 2-D cylindrical FDTD model developed by Hu and Cummer [18].

In this work, we expand their 2-D, tightly coupled E-J collocation plasma method to the fully 3-D case. As a result, taking into account all three particle species (electrons, positive ions, and negative ions), our whole 3-D iteration system consists of 15 linear equations with 15 state variables. We use an equivalent set of explicit iteration equations to derive the FDTD iteration coefficients for these 15 linear equations (rather than deriving them analytically). Unlike for a 2-D plasma code, using our newly developed 3-D FDTD anisotropic plasma model, we are able to model such effects as Faraday rotation and complete 3-D spatial variations of the magnetized cold plasma. Our simulation results for Faraday rotation and EM propagation characteristics agree very well with plasma theory.

Ongoing work includes extending the 3-D plasma algorithm developed here to the latitude-longitude [30] and geodesic [31] global 3-D FDTD models of the Earth-ionosphere waveguide. These global models could greatly improve simulation capabilities and results for a wide variety of applications, such as those described in [32] or [33].

APPENDIX

Iteration Matrix A: see the matrix at the bottom of the page.

Iteration Matrix B: see the first matrix at the top of the following page.
Iteration Matrix C: see the second matrix at the top of the following page.

ACKNOWLEDGMENT

$$\begin{bmatrix}
1 & 0 & 0 & 0.5 & 0.5 & 0.5 & 0 & 0 & 0 & 0 & 0 & 0 \\
0 & 1 & 0 & 0 & 0 & 0 & 0.5 & 0.5 & 0.5 & 0 & 0 & 0 \\
0 & 0 & 1 & 0 & 0 & 0 & 0 & 0 & 0 & 0.5 & 0.5 & 0.5 \\
-\frac{(\omega_{Pe}dt)^2}{2} & 0 & 0 & 1+\frac{\nu_e dt}{2} & 0 & 0 & \frac{\omega_{Cez}dt}{2} & 0 & 0 & -\frac{\omega_{Cey}dt}{2} & 0 & 0 \\
-\frac{(\omega_{Pp}dt)^2}{2} & 0 & 0 & 0 & 1+\frac{\nu_p dt}{2} & 0 & 0 & -\frac{\omega_{Cpz}dt}{2} & 0 & 0 & \frac{\omega_{Cpy}dt}{2} & 0 \\
-\frac{(\omega_{Pn}dt)^2}{2} & 0 & 0 & 0 & 0 & 1+\frac{\nu_n dt}{2} & 0 & 0 & \frac{\omega_{Cnz}dt}{2} & 0 & 0 & -\frac{\omega_{Cny}dt}{2} \\
0 & -\frac{(\omega_{Pe}dt)^2}{2} & 0 & -\frac{\omega_{Cez}dt}{2} & 0 & 0 & 1+\frac{\nu_e dt}{2} & 0 & 0 & \frac{\omega_{Cex}dt}{2} & 0 & 0 \\
0 & -\frac{(\omega_{Pp}dt)^2}{2} & 0 & 0 & \frac{\omega_{Cpz}dt}{2} & 0 & 0 & 1+\frac{\nu_p dt}{2} & 0 & 0 & -\frac{\omega_{Cpx}dt}{2} & 0 \\
0 & -\frac{(\omega_{Pn}dt)^2}{2} & 0 & 0 & 0 & -\frac{\omega_{Cnz}dt}{2} & 0 & 0 & 1+\frac{\nu_n dt}{2} & 0 & 0 & \frac{\omega_{Cnx}dt}{2} \\
0 & 0 & -\frac{(\omega_{Pe}dt)^2}{2} & \frac{\omega_{Cey}dt}{2} & 0 & 0 & -\frac{\omega_{Cex}dt}{2} & 0 & 0 & 1+\frac{\nu_e dt}{2} & 0 & 0 \\
0 & 0 & -\frac{(\omega_{Pp}dt)^2}{2} & 0 & -\frac{\omega_{Cpy}dt}{2} & 0 & 0 & \frac{\omega_{Cpx}dt}{2} & 0 & 0 & 1+\frac{\nu_p dt}{2} & 0 \\
0 & 0 & -\frac{(\omega_{Pn}dt)^2}{2} & 0 & \frac{\omega_{Cny}dt}{2} & 0 & 0 & -\frac{\omega_{Cnx}dt}{2} & 0 & 0 & 1+\frac{\nu_n dt}{2}
\end{bmatrix}$$

$$\begin{bmatrix}
1 & 0 & 0 & -0.5 & -0.5 & -0.5 & 0 & 0 & 0 & 0 & 0 & 0 \\
0 & 1 & 0 & 0 & 0 & 0 & -0.5 & -0.5 & -0.5 & 0 & 0 & 0 \\
0 & 0 & 1 & 0 & 0 & 0 & 0 & 0 & 0 & -0.5 & -0.5 & -0.5 \\
\frac{(\omega_{Pe}dt)^2}{2} & 0 & 0 & 1-\frac{\nu_e dt}{2} & 0 & 0 & -\frac{\omega_{Cez}dt}{2} & 0 & 0 & \frac{\omega_{Cey}dt}{2} & 0 & 0 \\
\frac{(\omega_{Pp}dt)^2}{2} & 0 & 0 & 0 & 1-\frac{\nu_p dt}{2} & 0 & 0 & \frac{\omega_{Cpz}dt}{2} & 0 & 0 & -\frac{\omega_{Cpy}dt}{2} & 0 \\
\frac{(\omega_{Pn}dt)^2}{2} & 0 & 0 & 0 & 0 & 1-\frac{\nu_n dt}{2} & 0 & 0 & -\frac{\omega_{Cnz}dt}{2} & 0 & 0 & \frac{\omega_{Cny}dt}{2} \\
0 & \frac{(\omega_{Pe}dt)^2}{2} & 0 & \frac{\omega_{Cez}dt}{2} & 0 & 0 & 1-\frac{\nu_e dt}{2} & 0 & 0 & -\frac{\omega_{Cex}dt}{2} & 0 & 0 \\
0 & \frac{(\omega_{Pp}dt)^2}{2} & 0 & 0 & -\frac{\omega_{Cpz}dt}{2} & 0 & 0 & 1-\frac{\nu_p dt}{2} & 0 & 0 & \frac{\omega_{Cpx}dt}{2} & 0 \\
0 & \frac{(\omega_{Pn}dt)^2}{2} & 0 & 0 & 0 & \frac{\omega_{Cnz}dt}{2} & 0 & 0 & 1-\frac{\nu_n dt}{2} & 0 & 0 & -\frac{\omega_{Cnx}dt}{2} \\
0 & 0 & \frac{(\omega_{Pe}dt)^2}{2} & -\frac{\omega_{Cey}dt}{2} & 0 & 0 & \frac{\omega_{Cex}dt}{2} & 0 & 0 & 1-\frac{\nu_e dt}{2} & 0 & 0 \\
0 & 0 & \frac{(\omega_{Pp}dt)^2}{2} & 0 & \frac{\omega_{Cpy}dt}{2} & 0 & 0 & -\frac{\omega_{Cpx}dt}{2} & 0 & 0 & 1-\frac{\nu_p dt}{2} & 0 \\
0 & 0 & \frac{(\omega_{Pn}dt)^2}{2} & 0 & 0 & -\frac{\omega_{Cny}dt}{2} & 0 & 0 & \frac{\omega_{Cnx}dt}{2} & 0 & 0 & 1-\frac{\nu_n dt}{2}
\end{bmatrix} \cdot$$

$$\begin{bmatrix}
\frac{dt^2}{\varepsilon_0\mu_0 dz} & -\frac{dt^2}{\varepsilon_0\mu_0 dy} & 0 & 0 & 0 & 0 & -1 & 0 & 0 \\
0 & 0 & \frac{dt^2}{\varepsilon_0\mu_0 dx} & -\frac{dt^2}{\varepsilon_0\mu_0 dz} & 0 & 0 & 0 & -1 & 0 \\
0 & 0 & 0 & 0 & \frac{dt^2}{\varepsilon_0\mu_0 dy} & -\frac{dt^2}{\varepsilon_0\mu_0 dx} & 0 & 0 & -1 \\
0 & 0 & 0 & 0 & 0 & 0 & 0 & 0 & 0 \\
0 & 0 & 0 & 0 & 0 & 0 & 0 & 0 & 0 \\
0 & 0 & 0 & 0 & 0 & 0 & 0 & 0 & 0 \\
0 & 0 & 0 & 0 & 0 & 0 & 0 & 0 & 0 \\
0 & 0 & 0 & 0 & 0 & 0 & 0 & 0 & 0 \\
0 & 0 & 0 & 0 & 0 & 0 & 0 & 0 & 0 \\
0 & 0 & 0 & 0 & 0 & 0 & 0 & 0 & 0 \\
0 & 0 & 0 & 0 & 0 & 0 & 0 & 0 & 0 \\
0 & 0 & 0 & 0 & 0 & 0 & 0 & 0 & 0
\end{bmatrix} \cdot$$

REFERENCES

[1] K. Yee, "A numerical solution of initial boundary value problems involving Maxwell's equations in isotropic media," *IEEE Trans. Antennas Propag.*, vol. 14, pp. 302–307, 1966.

[2] A. Taflove and S. C. Hagness, *Computational Electromagnetics: Finite-Difference Time-Domain Method*, 3rd ed. Norwood, MA: Artech House, 2005.

[3] R. J. Luebbers, F. Hunsberger, and K. S. Kunz, "A frequency-dependent finite-difference time-domain formulation for transient propagation in a plasma," *IEEE Trans. Antennas Propag.*, vol. 39, pp. 29–34, Jan. 1991.

[4] L. J. Nickisch and P. M. Franke, "Finite-difference time-domain solution of Maxwell's equations for the dispersive ionosphere," *IEEE Antennas Propag. Mag.*, vol. 34, pp. 33–39, Oct. 1992.

[5] J. L. Young, "A full finite difference time domain implementation for radio wave propagation in a plasma," *Radio Sci.*, vol. 29, pp. 1513–1522, 1994.

[6] J. L. Young, "A higher order FDTD method for EM propagation in a collisionless cold plasma," *IEEE Trans. Antennas Propag.*, vol. 44, pp. 1283–1289, Sep. 1996.

[7] Q. Chen, M. Katsurai, and P. H. Aoyagi, "An FDTD formulation for dispersive media using a current density," *IEEE Trans. Antennas Propag.*, vol. 46, pp. 1739–1746, Oct. 1998.

[8] J. Zhonghe *et al.*, "Propagation of electromagnetic TM (S-polarization) mode in two-dimensional atmospheric plasma," *Plasma Sci. Tech.*, vol. 8, pp. 297–299, May 2006.

[9] G. Bin, W. Xiaogang, and Z. Yu, "FDTD numerical simulation of absorption of microwaves in an unmagnetized atmosphere plasma," *Plasma Sci. Tech.*, vol. 8, pp. 558–560, Sep. 2006.

[10] D. F. Kelley and R. J. Luebbers, "Piecewise linear recursive convolution for dispersive media using FDTD," *IEEE Trans. Antennas Propag.*, vol. 44, pp. 792–797, Jun. 1996.

[11] D. M. Sullivan, "Z-transform theory and the FDTD method," *IEEE Trans. Antennas Propag.*, vol. 44, pp. 28–34, Jan. 1996.

[12] S. A. Cummer, "An analysis of new and existing FDTD methods for isotropic cold plasma and a method for improving their accuracy," *IEEE Trans. Antennas Propag.*, vol. 45, pp. 392–400, 1997.

[13] M. Cho and M. J. Rycroft, "Computer simulation of the electric field structure and optical emission from cloud-top to the ionosphere," *J. Atoms. Terr. Phys.*, vol. 60, pp. 871–888, 1998.

[14] V. P. Pasko, U. S. Inan, T. F. Bell, and S. C. Reising, "Mechanism of ELF radiation from sprites," *Geophys. Res. Lett.*, vol. 25, pp. 3493–3496, 1998.

[15] G. Veronis, V. P. Pasko, and U. S. Inan, "Characteristics of mesospheric optical emissions produced by lightning discharges," *J. Geophys. Res.*, vol. 104, pp. 12 645–12 656, 1999.

[16] S. A. Cummer, "Modeling electromagnetic propagation in the earth-ionosphere waveguide," *IEEE Trans. Antennas Propag.*, vol. 48, pp. 1420–1429, 2000.

[17] M. Thèvenot, J. P. Bérenger, T. Monedière, and F. Jecko, "A FDTD scheme for the computation of VLF-LF propagation in the anisotropic earth-ionosphere waveguide," *Ann. Télécommun.*, vol. 54, pp. 297–310, 1999.

[18] W. Hu and S. A. Cummer, "An FDTD model for low and high altitude lightning-generated EM fields," *IEEE Trans. Antennas Propag.*, vol. 54, pp. 1513–1522, May 2006.

[19] W. Hu, S. A. Cummer, and W. A. Lyons, "Testing sprite initiation theory using lightning measurements and modeled electromagnetic fields," *J. Geophys. Res.*, vol. 112, pp. 12645–12656, 2007.

[20] J. L. Young, A. Kittichartphayak, Y. M. Kwok, and D. Sullivan, "On the dispersion errors related to (FD)2TD type schemes," *IEEE Trans. Microw. Theory Tech.*, vol. 43, pp. 1902–1909, 1995.

[21] J. H. Lee and D. K. Kalluri, "Three dimensional FDTD simulation of electromagnetic wave transformation in a dynamic inhomogeneous magnetized plasma," *IEEE Trans. Antennas Propag.*, vol. 47, pp. 1148–1151, 1999.

[22] L. Xu and N. Yuan, "FDTD formulations for scattering from 3-D anisotropic magnetized plasma objects," *IEEE Antennas Wirless Propag. Lett.*, vol. 5, pp. 335–338, 2006.

[23] S. Liu and S. Liu, "Runge-Kutta exponential time differencing FDTD method for anisotropic magnetized plasma," *IEEE Antennas Wireless Propag. Lett.*, vol. 7, pp. 306–309, 2008.

[24] J. A. Payne, U. S. Inan, F. R. Foust, T. W. Chevalier, and T. F. Bell, "HF modulated ionospheric currents," *Geophys. Res. Lett.*, vol. 34, L23101, 2007.

[25] Personal Communication Apr. 21, 2009.

[26] T. W. Chevalier, U. S. Inan, and T. F. Bell, "Terminal impedance and antenna current distribution of a VLF electric dipole in the inner magnetosphere," *IEEE Trans. Antennas Propag.*, vol. 56, pp. 2454–2468, Aug. 2008.

[27] F. Hunsberger, R. Luebbers, and K. Kunz, "Finite-Difference time-domain analysis of gyrotropic media-I: Magnetized plasma," *IEEE Trans. Antennas Propag.*, vol. 40, pp. 1489–1495, Dec. 1992.

[28] S. J. H. Huang and F. Li, "FDTD simulation of electromagnetic propagation in magnetized plasma using z-transforms," *International Journal of Infrared Millimeter Waves*, vol. 25, no. 5, pp. 815–825, May 2004.

[29] F. C. Francis, *Introduction to Plasma Physics and Controlled Fusion*, 2nd ed. New York and London: Plenum Press, 1984.

[30] J. J. Simpson and A. Taflove, "Three-dimensional FDTD modeling of impulsive ELF antipodal propagation and Schumann resonance of the earth-sphere," *IEEE Trans. Antennas Propag.*, vol. 52, pp. 443–451, Feb. 2004.

[31] J. J. Simpson, R. P. Heikes, and A. Taflove, "FDTD modeling of a novel ELF radar for major oil deposits using a three-dimensional geodesic grid of the earth-ionosphere waveguide," *IEEE Trans. Antennas Propag.*, vol. 54, pp. 1734–1741, Jun. 2006.

[32] J. J. Simpson and A. Taflove, "A review of progress in FDTD Maxwell's equations modeling of impulsive sub-ionospheric propagation below 300 kHz," *IEEE Trans. Antennas Propag.: Special Issue on Electromagn. Wave Propa. Complex Environments: A Tribute to Leopold Benno Felsen*, vol. 55, no. 6, pp. 1582–1590, Jun. 2007.

[33] J. J. Simpson, "Current and future applications of full-vector 3-D Maxwell's equations FDTD global earth-ionosphere waveguide models," *Surveys Geophys.*, vol. 30, no. 2, pp. 105–130, 2009.

Yaxin Yu received the B.S. degree in physics from Northwest University, China, in 2000, the M.S. degree in optics from Nankai University, China, in 2003, and the M.S. degree in electrical engineering from the University of New Mexico, Albuquerque, in 2006, where he is currently working toward the Ph.D. degree.

His research interests include semiconductor optoelectronics, especially the III–V compound semiconductor materials and devices, and the finite-difference time-domain (FDTD) solution of Maxwell's equations. His current research focuses on FDTD simulation of electromagnetic wave propagation in ionosphere.

Jamesina J. Simpson (S'01–M'07) received the B.S. and Ph.D. degrees from Northwestern University, Evanston, IL, in 2003 and 2007, respectively.

She joined the Electrical and Computer Engineering Department, University of New Mexico, Albuquerque, as an Assistant Professor in August 2007. Her research focuses on the finite-difference time-domain (FDTD) solution of Maxwell's equations. To date, her work has spanned applications ranging from geophysically induced electromagnetic propagation and phenomena in the Earth-ionosphere system, to electromagnetic compatibility issues arising in compact portable electronic devices and to optical interactions with living tissues.

Dr. Simpson is a member of Tau Beta Pi and received the National Science Foundation Graduate Research Fellowship, Walter P. Murphy Fellowship, IEEE AP-S Graduate Research Award, and IEEE MTT-S Graduate Fellowship to support her graduate studies. She was also awarded the 2007 Best Ph.D. Dissertation Award from the Northwestern Electrical Engineering and Computer Science Department.